CrossMark

Rapid ascent and emplacement of basaltic lava during the 2005–06 eruption of the East Pacific Rise at ca. 9°51′N as inferred from CO_2 contents

J.E. Gardner [a,*], B.A. Jackson [a], H. Gonnermann [b], S.A. Soule [c]

[a] *Department of Geological Sciences, Jackson School of Geosciences, The University of Texas at Austin, Austin, TX, 78712-0254, USA*
[b] *Department of Earth Science, Rice University, Houston, TX, 77005, USA*
[c] *Woods Hole Oceanographic Institution, Department of Geology and Geophysics, Woods Hole, MA, 02536, USA*

ABSTRACT

Eruption rates at the mid-ocean ridges (MORs) are believed to strongly control the morphology and length of lava flows emplaced along the ridge axis, and thus the structure and porosity of the upper oceanic crust. Eruption rate also represents one of the few tools to gain insight into the driving pressures within sub-ridge magmatic systems. As eruption rate is inferred to vary systematically along the global mid-ocean ridge system, understanding of how to assess eruption rate in submarine systems and how it maps to observable features of the ridge axis would provide a powerful tool to understand Earth's largest magmatic system. Eruption rates at MORs are poorly constrained, however, because of a lack of direct observations, preventing the duration of an eruption to be quantified. This study uses decompression experiments of MORB samples and numerical modeling of CO_2 degassing to reconstruct the timescales for magma ascent and lava emplacement during the 2005–06 eruption of the East Pacific Rise at ca. 9°51′N. Samples collected from the lava flow are all supersaturated in dissolved CO_2 contents, but CO_2 decreases with distance from the vent, presumably as a consequence of progressive CO_2 diffusion into growing bubbles. Samples collected at the vent contain $\sim 10^5$ vesicles per cm^3. Pieces of these samples were experimentally heated to 1225 °C at high pressure and then decompressed at controlled rates. Results, plus those from numerical modeling of diffusive bubble growth, indicate that magma rose from the axial magma chamber to the seafloor in ≤ 1 h and at a rate of ≥ 2–3 $km\,h^{-1}$. Our modeling, as validated by experimental decompression of MORB samples with $\sim 10^6$ vesicles cm^{-3}, also suggests that CO_2 degassed from the melt within ~ 10–100 min as the vesicular lava traveled ~ 1.7 km along the seafloor, implying a volumetric flow rate on order of $10^{3–4}$ $m^3\,s^{-1}$. Given an ascent rate of ≥ 0.2 $m\,s^{-1}$, the width of a rectangular dike feeding the lava would have been ~ 1–2 m wide. MORB samples from the Pacific ridge are generally more supersaturated in dissolved CO_2 than those from slower spreading Atlantic and Indian ridges. Our results suggest that Pacific MORBs ascend to the seafloor faster than Atlantic or Indian MORBs.

© 2016 Elsevier B.V. All rights reserved.

1. Introduction

The morphology of submarine lava flows, typically of basaltic composition, ranges from pillow through lobate to sheet flows, and is thought to reflect an increase in eruptive rate, with pillow lavas formed at low eruptive rates and sheet flows at high rates (Gregg and Fink, 1995; Soule et al., 2005; Fundis et al., 2010; Chadwick et al., 2013). It has been found that globally the morphology of mid-ocean ridge basalt (MORB) flows varies with spreading rate, with fast spreading ridges dominated by sheet flows and slow spreading ridges having mainly pillow lavas (Bonatti and Harrison, 1988; Perfit and Chadwick, 1998). Although this correlation is presumably a consequence of eruption rate, it remains unclear whether faster eruption rates reflect a greater rate of magma supply to the axial magma chamber along fast spreading ridges.

While lava morphology may reflect eruptive dynamics, it does not quantify eruption rates, because the time scales for magma ascent and lava emplacement are unknown. Estimating those times could, however, be possible from the dissolved CO_2 in MORB coupled with vesicularity characteristics (Paonita and Martelli, 2006; Soule et al., 2012; Chavrit et al., 2012). MORB is often supersat-
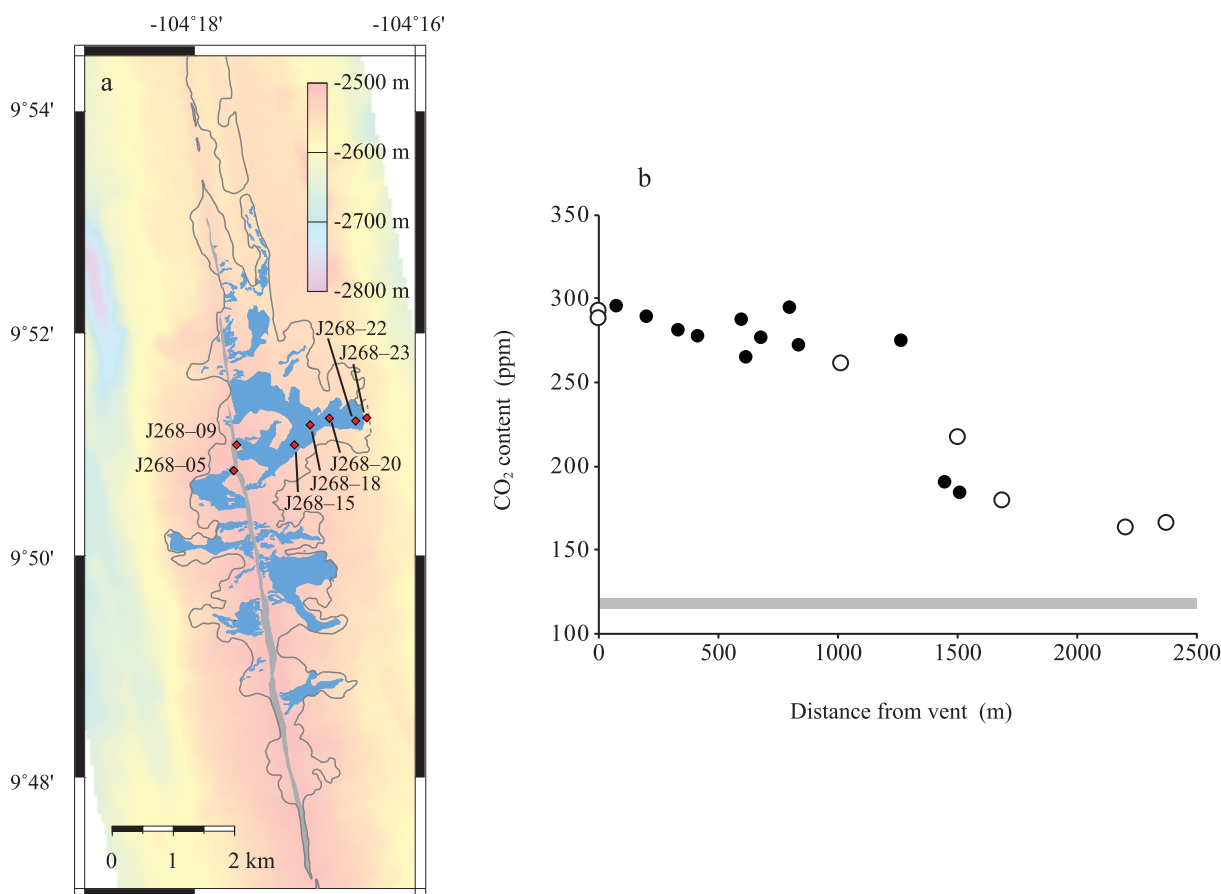
Fig. 1. a) Map showing positions of samples used in this study, collected from the central portion of the 2005–06 EPR eruption (gray line) with distributary channel systems (blue) comprised of smooth sheet and hackly sheet flows (modified from Soule et al., 2012). Eruptive vents are located within the narrow axial summit trough (light gray). Color shows seafloor depth. **b)** Variation in dissolved CO_2 content in lava samples as a function of distance from vent. Open symbols are samples scanned by high-resolution X-ray computed tomography in this study. The saturation value of CO_2 for the ambient seafloor pressure is shown as a gray bar. (For interpretation of the references to color in this figure legend, the reader is referred to the web version of this article.)

urated in CO_2 (e.g., Fine and Stolper, 1986; Dixon et al., 1988; Simons et al., 2002; Shaw et al., 2010; Soule et al., 2012), presumably because of the relatively slow diffusivity of CO_2, in combination with low bubble number density (N_V), which results in relatively large diffusion times. Consequently, during lava-flow emplacement, these CO_2 concentrations may gradually decrease from supersaturated to equilibrium conditions, resulting from CO_2 diffusion into existing bubbles as the bubbly lava flows away from the vent. Previous models for estimating magma ascent rates at the mid-ocean ridge have mainly been based on kinetic fractionation of noble gases and supersaturation of CO_2 during MORB degassing, because of the different diffusivities of the gas species (e.g., Sarda and Graham, 1990; Burnard, 1999; Aubuad et al., 2004; Hanyu et al., 2005; Paonita and Martelli, 2006; Soule et al., 2012; Chavrit et al., 2012). These models generally agree that ascent rates range from ∼0.05 to 10 m s^{-1}. Differences exist between model predictions, however, when focused on similar MORB samples, and apparently arise partly from differences in the vesicle populations assumed in the modeling (e.g., Chavrit et al., 2012). Despite such differences, the link between volatile contents and eruptive rates provides a promising way of establishing the eruption dynamics of submarine lava flows.

This study follows some of these previous ones (e.g., Paonita and Martelli, 2006; Soule et al., 2012; Chavrit et al., 2012) by focusing on the supersaturation CO_2. Unlike most previous studies, however, we focus on the evolution of CO_2 supersaturation in a single lava flow in order to infer both ascent and extrusion rates from the degassing time scales for the 2005–06 eruption at the

East Pacific Rise (Soule et al., 2012). In addition, we validate the modeling with suites of MORB samples that were decompressed experimentally. We show that the number density of vesicles in MORB strongly control the rate of degassing, and thus show that dissolved gas contents must be coupled with vesicularity characteristics to infer magma ascent and lava emplacement of MORB.

2. Vesicle populations in 2005–06 lava samples

Soule et al. (2012) examined samples collected closely spaced along two transects from vent to flow front of the 2005–06 lava located near the along-axis center of the eruptive fissure along the East Pacific Rise (EPR) (Fig. 1). Vesicles are found in all samples (Fig. 2), and the surrounding glass is supersaturated in CO_2 by a factor of up to 2.5 times the amount expected at the depth of the seafloor. The degree of super-saturation, however, decreases with distance from the vent. Detailed analyses of He abundances show that the fluid contained in the vesicles resulted from closed-system degassing. Consequently, it is reasonable to assume that the decrease in CO_2 resulted from progressive diffusion of CO_2 into bubbles as the lava flowed along the seafloor. Samples from the vent have CO_2 contents that match those expected at saturation at the pressure of the axial magma chamber below (Soule et al., 2012). Almost all loss of CO_2 to vesicles thus occurred on the seafloor, as opposed to during ascent from magma chamber to the surface.

A subset of the samples studied by Soule et al. (2012) that cover the range of measured CO_2 contents were analyzed for the num-

Table 1
Volatile contents and vesicles populations in samples from 2005–06 EPR lava flow[a].

Sample	Flow distance (m)	CO_2[b] (ppm)	CO_2[c] (ppm)	H_2O[b] (wt.%)	H_2O[c] (wt.%)	Vesicularity[d] (vol.%)	N_V[d] (cm^{-3})	Average diameter[d] (μm)	n[d]
J268-05	0	293.2	327 ± 25	0.180	0.19 ± 0.01	0.005	$10^{5.21}$	7 ± 3	231
J268-09	0	288.1	284 ± 59	0.150	0.17 ± 0.02	0.012	$10^{5.11}$	9 ± 5	1799
J268-10	80	295.1	251 ± 24	0.151	0.16 ± 0.01	–	–	–	–
J268-11	337	281.1	–	0.182	–	–	–	–	–
J268-12	601	286.9	–	0.117	–	–	–	–	–
J268-13	685	276.3	–	0.167	–	–	–	–	–
J268-14	802	294.0	–	0.171	–	–	–	–	–
J268-15	1016	261.0	–	0.162	–	0.066	$10^{5.58}$	11 ± 7	4433
J268-16	1270	275.3	–	0.177	–	–	–	–	–
J268-17	1450	189.8	–	0.178	–	–	–	–	–
J268-18	1500	216.8	–	0.170	–	0.35	$10^{6.25}$	10 ± 8	24016
J268-19	1515	184.2	–	0.169	–	–	–	–	–
J268-20	1695	179.1	–	0.182	–	0.33	$10^{5.27}$	23 ± 15	29713
J268-22	2207	162.8	–	0.193	–	0.37	$10^{6.05}$	9 ± 10	27746
J268-23	2378	165.6	–	0.189	–	0.44	$10^{6.47}$	7 ± 7	12534

[a] See Soule et al. (2012) for complete sample collection information. Flow distances are measured relative to the ridge axis.

[b] Dissolved CO_2 and H_2O contents reported in Soule et al. (2012), analyzed by secondary-ion mass spectrometry (SIMS). Uncertainties (2σ) are 10%.

[c] Dissolved CO_2 and H_2O contents measured in this study by Fourier Transform Infrared Spectrometry (FTIR), with 1σ uncertainties listed.

[d] Vesicularity (in vol.%), number density (N_V, in cm^{-3}), and average vesicle diameter (in μm) by this study from measuring n number of vesicles in combined analysis of samples in thin section and with high-resolution computed X-ray tomography (HR-XCT). See Appendix A for details.
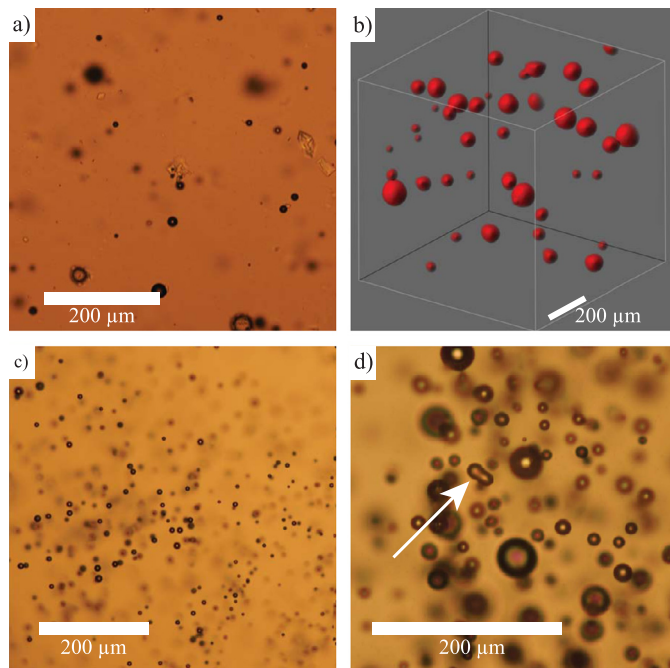

Fig. 2. Representative photomicrographs of natural and experimental samples. **a)** Photomicrograph of J268-18 showing vesicles in brown glass; **b)** rendition of sub-volume (∼0.37 mm^3) of high-resolution X-ray computed tomography scan of J268-18; **c)** photomicrograph of experiment M16; **d)** photomicrograph of M45, with arrow pointing to two bubbles partially merging together. Note all scale bars are 200 μm long.

Fig. 3. Mean vesicle diameter as a function of vesicularity, with curves showing how vesicle number density (N_V; in vesicles cm^{-3}) is related to vesicularity and diameter. Filled circles are the vesicularities and mean sizes of vesicles in the two vent samples (J268-05 and J268-09) from the 2005–06 EPR lava; open circles are those collected at different distances away from vent. Note that N_V implied for some distal samples exceed those measured, because the curves were calculated assuming all vesicles are the same size.

ber of vesicles per unit volume (vesicle number density; N_V). Each sample was analyzed optically in thick section to measure and count vesicles between ∼2–20 μm in diameter and analyzed by high-resolution computed X-ray tomography (HR-XCT) to measure and count larger vesicles; methods are described in Appendix A. Most samples come from one flow lobe, and include two vent samples (J268-05 and J268-09) and five collected between 1000 to 2378 m away from vent (Table 1). By combining methods, a total of 231–29,713 vesicles were measured in each sample, with the number being strongly controlled by sample size (Table 1). Overall, vesicles are spherical, and range in diameter from ∼2 to ∼450 μm, with mean sizes ranging from 7 to 23 μm (Fig. 3). The vent sam-
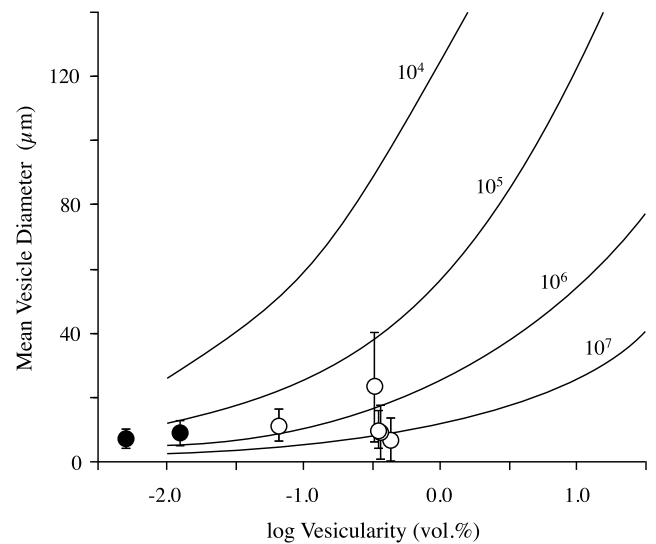
ples have similar vesicularities (vesicle volume fraction × 100), N_V values, and mean vesicle sizes (Table 1). Vesicularity increases with distance from the vent up to values of 0.44%, with a pronounced increase between ∼1000 and 1500 m. N_V also generally increases with distance, with the most distal samples having an order of magnitude more vesicles than vent samples. There is little change in the mean size of vesicles, but there are generally more vesicles larger than 30 μm in diameter in samples collected farther than ∼1000 m from vent than in samples closer to the vent. Indeed, the average size of the 10 largest vesicles in each sample increases by almost a factor of 3, from 48 μm to 137 μm, with distance from vent.

CO_2 contents dissolved in the glass generally decrease from the vent towards the flow front, with most of the decrease occurring between a distance of 800 and 1400 m from the vent (Table 1). While the decrease corresponds to an increase in vesicularity and

Table 2
Experimental conditions and results[a].

Run[a]	P_I[b] (MPa)	Time at P_I[b] (h)	P_F[c] (MPa)	Rate[c] (MPa s^{-1})	Time at P_F[c] (h)	[CO$_2$][d] (ppm)	[H$_2$O][d] (wt.%)	N_V[e] (cm^{-3})	n[e]	Size[e] (µm)
M8	71	1	71	n.a.	–	205 ± 33	0.038 ± 0.007	$10^{7.51}$	150	3 ± 2
M10	72	1	72	n.a.	–	244 ± 14	0.126 ± 0.006	$10^{6.95}$	150	2 ± 2
M12	71	1	71	n.a.	–	282 ± 13	0.122 ± 0.023	$10^{5.57}$	150	3 ± 3
M28	70	12	70	n.a.	–	244 ± 30	0.110 ± 0.002	$10^{5.85}$	150	5 ± 1
M29	70	12	25.1	0.01	0	205 ± 2	0.063 ± 0.002	$10^{6.00}$	150	21 ± 3
M36	70	12	25.1	0.04	0	245 ± 27	0.036 ± 0.001	$10^{5.41}$	118	16 ± 2
M43	70	12	25.1	0.75–1.50	1	120 ± 8	0.081 ± 0.001	$10^{6.44}$	150	14 ± 3
M45	70	1	25.1	0.75–1.50	1	78 ± 7	0.090 ± 0.006	$10^{6.61}$	150	6 ± 2
M16	70	1	25.1	0.75–1.50	3	121 ± 20	n.d.	$10^{6.86}$	150	8 ± 2
M19	70	1	25.1	0.75–1.50	7	102 ± 25	0.072 ± 0.004	$10^{5.69}$	150	5 ± 5

[a] See Appendix B for a detailed description of experimental methods; all run at 1225 °C. Experiments M8, M43, and M45 used cylinders cored from J268-10, all others used cores from J268-09.

[b] P_I is the initial pressure of the experiment, with the amount of time held at that pressure listed.

[c] P_F is the final pressure of the experiment, with the amount of time held at that pressure listed and the rate pressure was released to reach PF given; n.a. = not applicable for the four experiments not decompressed before quenching. Pressure was released in controlled steps for M29 and M36, with the average rate of release listed. Pressure was released in 30–60 s for M43, M45, M16, and M19, with the rate equaling the total pressure drop divided by 30–60 s.

[d] Dissolved volatile contents measured by FTIR, with 1a uncertainties listed; n.d. not detected.

[e] Number density (N_V) and average bubble size ($\pm 1\sigma$ uncertainties) measured in thin section from counting n number of bubbles, as described in Appendix B.

N_V, relatively low CO$_2$ contents in the glass can be found in samples with both low and high N_V values.

3. Experimental results

A suite of experiments was carried out to investigate the time scale of CO$_2$ degassing in bubble bearing basaltic liquid. Full experimental methods are described in Appendix B. Briefly, cylinders that were cored from glassy regions of samples J268-05 and J286-09 were equilibrated at 1225 °C and 70 MPa, and then pressure was decreased either relatively instantaneously or at a controlled rate down to 25.1 MPa, equivalent to the ambient pressure of the seafloor at the vent (Table 2). The glasses were then analyzed to establish how much CO$_2$ degassed from the melt to bubbles. Four samples (M8, M10, M12, and M28) were quenched at 70 MPa to characterize how the samples re-equilibrated to the experimental conditions, prior to being decompressed. Experiment M12 contains ∼$10^{5.6}$ bubbles cm^{-3} and CO$_2$ contents of 282 ± 13 ppm, both of which match the natural vent samples. The other three have lower CO$_2$ contents and more bubbles ($N_V = 10^{5.9-7.5}$ cm^{-3}). All four have lower H$_2$O contents than the natural samples. N_V correlates negatively with dissolved volatile contents, suggesting that new bubbles grew during re-equilibration at 70 MPa. The ranges seen in CO$_2$ and N_V at high pressure are considered when evaluating the results after decompressions.

Natural vent samples have only ∼0.1–0.2 vol.% crystals, and so the lava erupted at near liquidus conditions (Soule et al., 2012). All experiments run at 1225 °C produce crystal-free glass and bubbles (Fig. 2), whereas one experiment (not reported) run at 1175 °C was extensively crystallized. The liquidus is thus between 1175–1225 °C, which is consistent with thermodynamic modeling that places the liquidus at ∼1195 °C at 26 MPa (Soule et al., 2012). It is thus reasonable to assume that the experiments were run only ∼25 °C hotter than the natural magma, which should not significantly affect the results of our analysis.

Two samples (M29 and M36) were decompressed to 25.1 MPa at controlled rates of 0.01 and 0.04 MPa s^{-1} (Table 2), as described in Appendix B. These samples have N_V values that overlap with those in the natural samples (Table 1), and N_V values and dissolved H$_2$O contents that fall within the range of those of samples quenched at high pressure (Table 2). CO$_2$ contents in these samples decrease with slower decompression rate. Relative to the starting CO$_2$ contents, the CO$_2$ left dissolved in the melt decreases from ∼100% at 0.04 MPa s^{-1} to ∼84% at 0.01 MPa s^{-1} (Fig. 4).
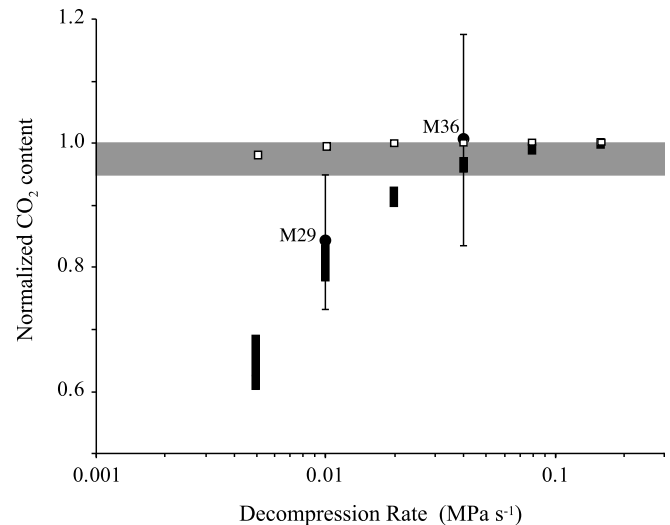

Fig. 4. Dissolved CO$_2$ contents normalized by the initial CO$_2$ content in experimental samples (black dots with sample numbers listed; see Table 2) and numerical runs (black and white bars) all plotted as functions of decompression rate. The numerical runs modeled decompression of the two vent samples separately at each decompression rate, with the vertical lengths of the bars covering the range of results; black bars are for $N_V \sim 10^5$ cm^{-3}; white bars, $N_V = 10^4$ cm^{-3}. Error bars associated with experimental samples result mainly from the uncertainty in the initial CO$_2$ contents of the experiments. The gray bar covers up to 5% loss of CO$_2$ from the starting values.

Four samples (M16, M19, M43, and M45; Table 2) were decompressed to 25.1 MPa almost instantaneously (∼30–60 s), as described in Appendix B. All samples have $10^{5.7-6.9}$ bubbles cm^{-3} and dissolved H$_2$O contents that fall within the ranges of those quenched at 70 MPa (Table 2). Although N_V values overlap, some coalescence of bubbles is seen (Fig. 2c). Dissolved CO$_2$ contents in these samples are, however, significantly less than those found at 70 MPa. In fact, other than M45, all samples have the same CO$_2$ content, averaging 120 ± 13 ppm. This concentration matches that expected from solubility at ∼25 MPa (Dixon et al., 1995).

CO$_2$ contents are greater in samples decompressed slowly compared to those decompressed quickly (Table 2). For example, the melt in M29 still has ∼205 ppm CO$_2$ dissolved in it after ∼1.25 h, whereas melt in M43 had degassed to ∼120 ppm in 1 h. There is no correlation of time held at low pressure with either dissolved H$_2$O content or final N_V, and importantly the range of values in all decompressed samples fall within the observed values at high
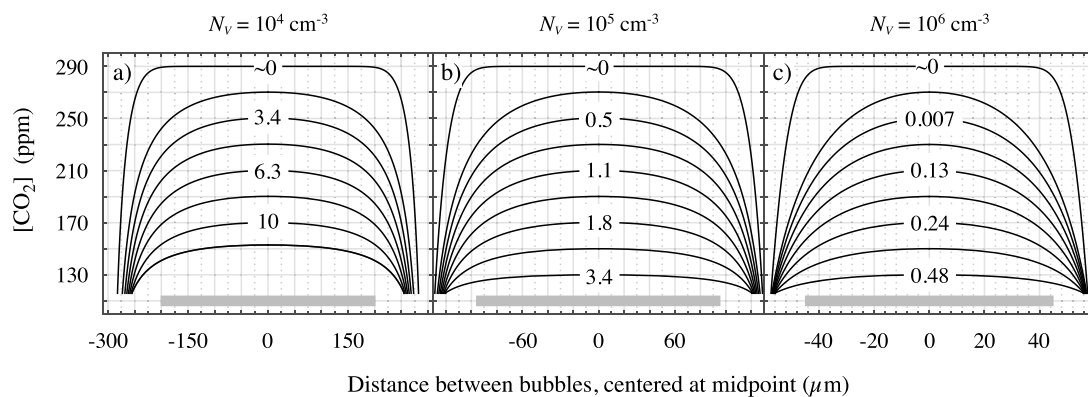
Fig. 5. Calculated CO_2 contents dissolved in the melt as a function of distance between two bubbles, with distance centered at the midpoint (r_{max} in the model) between them, for bubble number density (N_V) of **a)** 10^4 cm^{-3}, **b)** 10^5 cm^{-3}, and **c)** 10^6 cm^{-3} (labeled above each graph). Each curve shows the CO_2 contents after a specific amount of time (given in hours) has elapsed after degassing began. The length of the gray bar in each figure equals the middle $\sim$80% of the distance between bubbles, within which CO_2 typically varies by $\leq$10–20%.

pressure (Table 2). The difference thus likely results from a combination of slightly greater values of N_V in the rapidly decompressed samples and faster diffusive flux that results when pressure is dropped instantaneously (e.g., Zhang and Ni, 2010). These results are confirmed by our modeling as described below.

4. Numerical modeling of bubble growth

To investigate CO_2 degassing during magma ascent and lava emplacement, we develop a model for melt degassing in response to the growth of bubbles subjected to either continuous or instantaneous supersaturation. The model is based on the diffusive bubble growth formulation of Proussevitch and Sahagian (1998), adapted for a mixture of CO_2 and H_2O as first presented in Gonnermann and Manga (2005), and modified here using formulations for solubility (Dixon, 1997), fugacities and equation of state (Holloway, 1977; Flowers, 1979), CO_2 diffusivity (Zhang and Ni, 2010), H_2O diffusivity (Zhang and Ni, 2010), melt density (Lange, 1994; Ochs and Lange, 1999), and viscosity (Hui and Zhang, 2007; Lensky et al., 2001) suitable for the EPR basalt of this study. In all runs, bubbles are assumed to be distributed in uniform packing geometry (Proussevitch and Sahagian, 1998), such that each is approximated as a sphere surrounded by a spherical shell of melt of given thickness. It is also assumed that no bubbles nucleate during decompression or degassing.

In one set of numerical simulations, the initial condition is melt with CO_2 and H_2O contents and N_V set equal to those of the vent samples (Table 1). This assumes that all vesicles seen in the vent samples were present before magma ascent began. The melt–bubbles were then decompressed at controlled rates from 0.005 to 0.16 MPa s^{-1} to a final pressure equal to collection pressure of the vent samples. Although explicitly modeled, H_2O degassing is negligible because of its greater solubility. The amount of CO_2 left dissolved in the melt after reaching final pressure, relative to the starting amounts, increases systematically with decompression rate (Fig. 4). At 0.005 MPa s^{-1} only $\sim$60–68% of the CO_2 remains in the melt, but more than $\sim$96% remains at 0.04 MPa s^{-1} and faster. To examine the impact of N_V (i.e., vesicle spacing), a second set of numerical simulations were run with N_V set to 10^4 cm^{-3} (Fig. 4). Across the range of decompression rates, very little CO_2 is expected to degas from the melt. For example, at 0.005 MPa s^{-1} more than 97% of the initial dissolved CO_2 content remains in the melt. These results illustrate the importance of N_V (i.e., bubble spacing) to the timescale of degassing.

N_V in the slowly decompressed experiments (M29 and M36) are similar to those in the vent samples. Overall, model results agree well with our experimental results, despite large uncertainties in the absolute amounts of CO_2 lost in the experiments (Fig. 4). The timescales for degassing predicted by our model are thus consistent with our experimental results, and suggests that measurable loss of CO_2 from the melt will occur only at decompression rates of $\leq$0.05 MPa s^{-1} (assuming small uncertainties in analysis).

In the second set of numerical simulations, melt saturated in CO_2 at a pressure of 70 MPa (290 ppm CO_2) with $N_V = 10^4, 10^5$, and 10^6 cm^{-3} was decompressed instantaneously to 25 MPa and held there for various lengths of time. The rate at which bubbles grow varies with time, because the diffusive flux of CO_2 decreases as CO_2 concentration gradients between bubbles and melt change as a consequence of diffusion (Proussevitch and Sahagian, 1998). Because temperature and pressure are kept constant, the major control on the timescale for CO_2 degassing is the diffusion length squared; i.e., the thickness of melt separating adjacent bubbles, which scales as $N_V^{1/3}$. For a given value of N_V, melt thickness also depends on vesicularity, or equivalently bubble radius (Fig. 3).

We modeled CO_2 degassing for a range in N_V (Fig. 5). The concentration of CO_2 is shown as a function of distance between bubbles at different times. As can be seen, the melt closest to each bubble is quickly depleted in CO_2, whereas the far field melt loses CO_2 more slowly. The result is steep CO_2 gradients near bubbles and relatively shallow ones far away. Furthermore, the diffusion of CO_2 into the bubbles does not result in a significant increase in bubble size or vesicularity, because the relative increase in the mass of CO_2 per bubble is small. The maximum amount of dissolved CO_2 at any given time is found at the midpoint between bubbles (Fig. 6). When CO_2 contents at that position reach the saturation limit, the melt has equilibrated to low pressure. The difference in degassing times for different N_V is dramatic. When there are 10^4 bubbles cm^{-3}, for example, it takes $\sim$7 h for CO_2 at the midpoint to decrease from 290 to 200 ppm, but only $\sim$9 min when there are 10^6 bubbles cm^{-3}.

Before melt re-equilibrates, it will have some gradient in CO_2 content between bubbles (Fig. 5). If such melts are analyzed, then different amounts of CO_2 will be found at different positions. For the most part, however, gradients tend to be subdued away from bubbles, and in fact CO_2 varies by $\leq$10–20% over $\sim$80% of the distance between bubbles (Fig. 5). Therefore, as long as glasses are analyzed away from bubbles they should provide reasonable estimates of the maximum CO_2 content.

Numerical modeling predicts that melts supersaturated in CO_2 will degas at a rate depending on N_V (Figs. 5 and 6). The modeling assumes degassing in response to an initial supersaturation of $\sim$44 MPa. We can compare those predictions to our experimental samples decompressed quickly, which generated supersat-
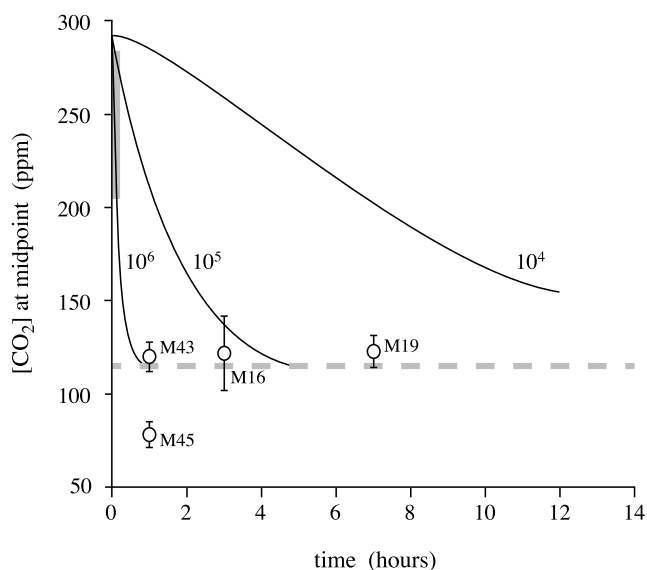
Fig. 6. Curves show variation in CO_2 contents at the midpoint (r_{max} in the model) between bubbles as a function of the amount of time (in hours) elapsed since degassing began. Bubble number density (N_V; in bubbles cm^{-3}) is listed next to each curve. The dashed line is the equilibrium CO_2 content at 25 MPa. When that value is reached at the midpoint, the melt has equilibrated. Open circles are CO_2 contents ($\pm 1\sigma$) in samples decompressed instantaneously to 25 MPa, plotted as a function of the amount of time spent at that pressure (sample numbers are listed next to each). The vertical gray bar at zero time covers the range of CO_2 contents in samples before being decompressed.

urations of $\sim$45 MPa (Table 2). These experiments have $N_V = 10^{5.7-6.9}$ cm^{-3}, and so we compare the experimental results to model predictions for $N_V = 10^6$ cm^{-3}, which predict that all gradients are eliminated and the melt is equilibrated within $\sim$1 h (Figs. 5 and 6). In fact, the instantaneously decompressed experimental samples have CO_2 contents that are in equilibrium at low pressure in $\leq$1 h (Fig. 6). The rapid timescale for degassing predicted by our model is thus consistent with our experimental results.

5. Discussion

Vesicles generally increase in number density (N_V) with distance from vent (Table 1). Jackson and Gardner (2015) found that much of that increase results from increased numbers of small vesicles, mainly $\leq$40 μm in diameter. The numbers of these smaller vesicles correlate with increased crystal numbers, and hence Jackson and Gardner (2015) propose that new vesicles nucleated while the lava traveled away from vent. Despite those greater numbers of small vesicles, much of the increased vesicularity results from increased sizes of large vesicles, which generally do not increase in number. Hence, most of the degassing of the matrix glass is by CO_2 diffusing into the large vesicles. Beyond ca. 1700 m away from vent (J268-20) the number of new vesicles become significant, and thus nucleation may be important in reducing CO_2 in the matrix. We thus restrict application of our modeling and growth experiments to examining degassing of the lava between the vent and ca. 1700 m away from vent (i.e., J268-20).

Results of our experiments and model predict that CO_2 in the basaltic melt will equilibrate to low pressure in less than 20 h when $N_V > 10^4$ cm^{-3}, which is faster than predictions by Soule et al. (2012). The difference most likely arises from the different growth models assumed. Soule et al. (2012) used a growth model based on an isolated bubble growing in an infinite melt, as opposed to the shell model used here. Very different growth rates occur between the two models (Barclay et al., 1995).

5.1. Ascent rates for MORB

The CO_2 contents in the vent samples equal those expected at saturation pressures of $\sim$62 MPa, which is roughly equivalent to that of the axial melt lens beneath the ridge (Soule et al., 2012). Assuming that the magma came from the melt lens, and that it had equilibrated prior to erupting, then it must have risen to the seafloor at a rate fast enough to prevent it from degassing.

Basalt decompressed experimentally at a controlled rate of 0.01 MPa s^{-1} lost $\sim$16% of the dissolved CO_2 (Fig. 4). On the other hand, the basalt decompressed at 0.04 MPa s^{-1} has CO_2 contents indistinguishable from the initial amounts. Model runs agree with the experimental results, and suggest that decompressions slower than 0.02 MPa s^{-1} result in significant ($\geq$10%) loss of CO_2 from the melt. Based on our FTIR analyses, there is $\sim$10% uncertainty in measured CO_2 contents in the vent samples (Table 1). In order for basalt to not lose 10% of its initial dissolved CO_2 during decompression, it would need to decompress faster than 0.02 MPa s^{-1}. We thus propose that the 2005–06 magma must have decompressed at a rate of $\geq$0.02 MPa s^{-1} to prevent significant amounts of CO_2 from degassing from the melt (Fig. 4). At a minimum, therefore, basaltic magma rose from the axial melt lens to the seafloor in $\leq$30 min ($\sim$36 MPa at $\geq$0.02 MPa s^{-1}). Given that the magma reservoir is $\sim$1400 m below the ridge (Kent et al., 1993; Soule et al., 2012), magma rose at $\geq$2–3 km h^{-1}, or $\geq$0.5–0.8 m s^{-1}. This rate is comparable to the $\geq$0.15 m s^{-1} estimated by Chavrit et al. (2012).

In a study of seismicity from the 2005–06 eruption of the EPR, Tolstoy et al. (2006) found that seismic amplitudes peaked over an hour-long interval at $\sim$1445 (GMT), in agreement with regional hydroacoustic data (Dziak et al., 2009). They suggest that during this period the primary dike rose from the axial magma chamber, implying a vertical propagation rate of $\sim$1400 m in one hour ($\sim$1.4 km h^{-1}). Magma ascent through the open dike should be $\geq$1.4 km h^{-1}, which agrees well with our estimate.

5.2. MORB degassing on the seafloor

Soule et al. (2012) argued that the slight increase in crystal content with distance from vent indicates that temperature cooled by only $\sim$2 °C km^{-1}. It is thus reasonable to assume that while the lava flowed along the seafloor it was within 5–10 °C of $\sim$1200 °C, which was assumed in the model. Most samples between the vent and 1700 m away have 10^5–10^6 bubbles cm^{-3}, with the vent samples having $10^{5.16 \pm 0.07}$ bubbles cm^{-3}. We thus bracket the degassing time scale using model results for $N_V = 10^5$ and 10^6 cm^{-3} (Figs. 5 and 6).

Between the vent and $\sim$1700 m away, CO_2 contents decrease from $\sim$290 ppm to $\sim$179 ppm (Fig. 1). Such degassing resulting from growth of $N_V = 10^{5-6}$ bubbles cm^{-3} would require $\sim$10–100 min (Fig. 6). That implies that the lava traveled $\sim$1.7 km at a speed of $\sim$1–10 km h^{-1}. As mentioned above, degassing beyond 1700 m may result at least partially from the nucleation of vesicles, and so it is unclear how fast the lava traveled once it was beyond 1700 m. An eruption duration of $\sim$10–100 min is, however, comparable to the "minutes to hours" duration estimated by Gregg et al. (1996) for the 1991 eruption along the same ridge segment of the EPR.

If the lava had flowed at a constant speed, then a plot of dissolved CO_2 content with distance would mimic that of dissolved CO_2 with time (Fig. 6). Dissolved CO_2 content does not, however, decrease monotonically with distance (Fig. 1). Instead, it decreases by $\leq$5 ppm across the first $\sim$800 m, then drops by $\sim$110 ppm over the next 900 m. About 85% of the CO_2 thus degassed between 800 and 1700 m. Such a dramatic change in degassing must

reflect a change in flow rate, degassing nature, or initial CO_2 contents, because little to no cooling occurred during flow (Soule et al., 2012). Soule et al. (2012) demonstrated, however, that overall changes in gas contents of the lava reflect closed-system degassing, which rules out large differences in initial gas content. In addition, while there are increased numbers of small bubbles in samples away from the vent, their increased numbers do not account for the decrease in CO_2 content. Indeed, much of the change in N_V in samples farther away than 1700 m results from nucleation, yet CO_2 contents decrease only ∼13 ppm in the last 700 m. The dramatic drop in dissolved CO_2 contents thus cannot be explained by bubble nucleation. We conclude that the variations in CO_2 contents across the lava reflect differences in its flow rate (that is, a non-constant speed), as suggested by Soule et al. (2012).

The amount of time that lava with 10^{5-6} vesicles cm^{-3} could travel 800 m away from the vent and the melt degas no more than 5 ppm CO_2 is ∼1–10 min (Fig. 6). The lowest CO_2 content found within 800 m of the vent is 265 ppm (Fig. 1), and so the most amount of time allowed is ∼1–20 min. Because N_V in the vent samples is closer to 10^5 cm^{-3}, it is likely that the longer times are more reasonable. The amount of time for the lava to travel over the next 900 m (800 to 1700 m) would be ∼10–90 min. Hence, while the overall decrease in CO_2 contents indicates that the lava traveled ∼1.7 km in less than two hours, its speed waned from ∼5–50 km h^{-1} in the first 800 m to ∼0.5–5 km h^{-1} over the next 900 m. Such a drop in spreading rate probably reflects either magma flux at the vent changing with time, growth of an impeding crust on the flow, or confluence of multiple channels impacting the flow.

6. Implications for MORB eruptions and conclusions

The timescales for magma ascent and lava emplacement during the 2005–06 eruption of the East Pacific Rise have been reconstructed through the use of targeted experimental results and numerical modeling. The supersaturated CO_2 contents of the vent samples require that magma ascended at a rate of ≥0.02 MPa s^{-1}, which corresponds to a vertical velocity of ≥2–3 km h^{-1}. The lava was then emplaced on the seafloor in ∼10–100 min, at a speed of ∼1–10 km h^{-1}. The lava slowed with distance, however, possibly reflecting slower magma flux at the vent or growth of a significant crust on the flow.

The volume of the 2005–06 EPR flow is ∼6 × 10^6 m^3 (Soule et al., 2007, 2012). If we assume that the entire volume was emplaced in ∼10–100 min, the average volumetric eruption rate was ∼10^{3-4} m^3 s^{-1}, or ∼$10^{2.5-3.7}$ m^3 s^{-1} km^{-1} of eruptive fissure. This estimated volumetric eruption rate overlaps the lower end of the 10^3–10^6 m^3 s^{-1} estimated for the 1991 lava (Gregg et al., 1996). The morphology of the 1991 and 2005–06 lavas are similar, although their volumes are different, suggesting that these types of lavas along the fast spreading East Pacific Rise erupt at rates on order of ≥10^3 m^3 s^{-1}. Given an eruption rate of ∼10^3 m^3 s^{-1} km^{-1} and an ascent rate of 0.5–0.8 m s^{-1}, the width of the dike feeding the lava would have been on order of 1–2 m wide (assuming a rectangular surface area). That width is comparable to dike widths seen in the Hess Deep rift and the Troodos ophiolite complex (Staudigel et al., 1992; Stewart et al., 2002), supporting the rates derived in this study.

The agreement between ascent rates estimated from dissolved CO_2 contents and seismicity is compelling evidence that volatile contents in MORB coupled with vesicularity characteristics can be used to infer ascent rate (e.g., Paonita and Martelli, 2006; Chavrit et al., 2012). In a study of volatile contents of MORB samples collected along the East Pacific Rise at 9–10°N and 12–14°N, le Roux et al. (2006) found that all on-axis samples were supersaturated in CO_2 contents, and that the majority of them had

volatile–saturated pressures equal to the local depth of the axial melt lens. Our results suggest that these magmas must rise to the seafloor at rates of ≥1 km h^{-1} in order to preserve those CO_2 concentrations, assuming they all have on order of 10^5 vesicles cm^{-3}. All of the samples have fewer than one percent of vesicles (le Roux et al., 2006). It thus appears that relatively rapid ascent is common along the fast spreading East Pacific Rise.

MORB erupted along the slower spreading Atlantic and Indian Ocean ridges are also supersaturated in CO_2, although not as commonly as along the faster spreading Pacific ridges (Chavrit et al., 2012). Vesicularities of Atlantic and Indian MORB are typically higher than Pacific MORB, however, and vesicles tend to occur in lower number densities (Chavrit et al., 2012). Importantly, the average spacing between vesicles in Atlantic and Indian MORB (∼480 and ∼560 μm) is almost twice as far as that in Pacific MORB (∼260 μm), as calculated from the vesicularities and N_V values presented by Chavrit et al. (2012). Our modeling indicates that degassing of MORB melt has a strong dependency on N_V (i.e., vesicle spacing). The greater values of N_V of Pacific MORB (Chavrit et al., 2012; this study) require that they rose relatively fast in order to preserve significant CO_2 supersaturations in the melt (Fig. 4). The lower degrees of supersaturation in Atlantic and Indian MORB, however, suggest significant degassing in these magmas and points to either slower ascent rates or much longer ascent paths to the seafloor. Our results stress that to examine magma ascent for MORB eruptions the density of vesicles (N_V), or more specifically the spacing between vesicles, must be well constrained.

Acknowledgements

Appendix A. Vesicle measurements

Vesicle sizes and number densities (N_V) within the quenched glassy rinds of EPR samples were measured using both optical and CT techniques (Fig. 2). Small portions (0.05–0.48 cm^3) of these glassy rinds were extracted and scanned using the Xradia MicroXCT scanner at the University of Texas, at Austin. Voxel sizes ranged from 5.73–7.15 μm in length. Vesicles within the CT scans were identified and measured using Blob3D software (Ketcham, 2005). Each was individually evaluated in Blob3D, and those that appeared touching were manually separated. A minimum size threshold of 6 voxels was used when segmenting vesicles, and so vesicles smaller than 13–16 μm in diameter (d) were not measured. Approximately 200–30,000 bubbles were measured in each sample, with the number of measured bubbles being strongly dictated by the size of the sample.

Optical measurements of vesicles were made using thick sections (90–190 μm thick) cut from the EPR samples. Vesicles as small as 1 μm could be resolved optically. For each sample, the diameter of ∼110–150 bubbles were measured. Total number densities of vesicles (N_V) measured by counting the number in a given area (between 60 μm × 60 μm to 600 μm × 600 μm) while focusing through the sample. Depth within a sample while focusing was measured using a Heidenhain focus drive linear encoder, and 5–10 unique regions were counted in each sample. Optical measurements were then merged with CT measurements by binning vesicles according to diameter, with bin intervals of 1 μm. The bins for each sample were then normalized using N_V.

Appendix B. Experimental techniques

All experiments used cylinders cored from the glassy regions of J268-05 and J286-10 (Table 1). Each sample consisted of one cylinder, typically ~1 cm long and ~2.7 mm in diameter, placed inside of a 3-mm O.D. $Au_{80}Pd_{20}$ capsule that was then welded shut. A sample was then loaded into a cold-seal MHC pressure vessel and then equilibrated at 1225 °C and 70 MPa for either 1 or 12 h. The pressurizing fluid was Ar plus ~0.1 MPa of CH_4. Four samples were quenched at high pressure following 1–12 h, whereas ten others were decompressed before being quenched. Six samples were decompressed down to 25 MPa in ~30–60 s, and held at that pressure for 1 to 7 h before being quenched; these are referred to as "instantaneous" decompressions. Two others, referred to as "slow decompressions", were decompressed at controlled rates and then quenched upon reaching 25 MPa. In these, the decompression was achieved by releasing pressure in steps of either 0.3 or 1.2 MPa every ~60 s. The samples were quenched in a matter of seconds, by pulling the pressure vessel out of the furnace and inverting it, causing the sample to fall from the hot zone into the water-cooled end.

Once removed from their capsules, samples were sectioned and doubly polished to analyze dissolved CO_2 and H_2O contents via Fourier-Transform Infrared spectroscopy (FTIR), with a Thermo Electron Nicolet 6700 spectrometer and Continuμm IR microscope. Both CO_2 and H_2O were measured from absorbances in mid-IR, using a KBr beamsplitter and globular light source. Carbon dissolved as carbonate was measured at ~1515 cm^{-1} and converted to CO_2 contents using a molar absorptivity of 375 l mol^{-1} cm^{-1}, following Fine and Stolper (1986). A separate IR peak for carbonate at ~1430 cm^{-1} (part of the carbonate doublet) was disregarded, as a result of interference from vibrations of the glass matrix (Fine and Stolper, 1986) near that wavenumber. Total H_2O (combination of molecular and hydroxyl H_2O) was measured using absorbance at ~3550 cm^{-1}, assuming a molar absorptivity of 63 l mol^{-1} cm^{-1} (Dixon et al., 1988). Backgrounds for peak height measurements of FTIR spectra were extrapolated linearly for the 3550 cm^{-1} peak and along a curve for the 1515 cm^{-1} peak, fitted using a French curve. The thickness of the sample where each analysis was analyzed was measured using a petrographic microscope by focusing on the top and bottom of the sample and recording how much the stage moved vertically with a Heidenhain focus drive linear encoder.

Bubbles were measured optically in all samples using a petrographic microscope, following the same techniques as for measuring vesicles in the natural samples (Appendix A). Number densities were measured by selecting multiple areas (up to 31 separate areas) that ranged between 120 μm × 120 μm to 2358 μm × 2358 μm of a sample and counting all bubbles that appear as the field of view is moved through it using the focusing knob of the microscope. The thickness of each volume measured was recorded by the focus drive linear encoder, and varied between 81 and 580 μm.

References

Aubuad, C., Pineau, F., Jambon, A., Javoy, M., 2004. Kinetic disequilibrium of C, He, Ar and carbon isotopes during degassing of mid-ocean ridge basalts. Earth Planet. Sci. Lett. 222, 391–406.

Barclay, J., Riley, D.S., Sparks, R.S.J., 1995. Analytical models for bubble growth during decompression of high viscosity magmas. Bull. Volcanol. 57, 422–431.

Bonatti, E., Harrison, C., 1988. Eruption styles of basalt in oceanic spreading ridges and seamounts: effect of magma temperature and viscosity. J. Geophys. Res. 93 (B4), 2967–2980.

Burnard, P., 1999. Eruption dynamics of "popping rock" from vesicle morphologies. J. Volcanol. Geotherm. Res. 92, 247–258.

Chadwick Jr., W.W., Clague, D.A., Embley, R.W., Perfit, M.R., Butterfield, D.A., Caress, D.W., Paduan, J.B., Martin, J.F., Sasnett, P., Merle, S.G., Bobbitt, A.M.,

2013. The 1998 eruption of axial seamount: new insights on submarine lava flow emplacement from high-resolution mapping. Geochem. Geophys. Geosyst. http://dx.doi.org/10.1002/ggge.20202.

Chavrit, D., Humler, E., Morizet, Y., Laporte, D., 2012. Influence of magma ascent rate on carbon dioxide degassing at oceanic ridges: message in a bubble. Earth Planet. Sci. Lett. 357–358, 376–385.

Dixon, J.E., 1997. Degassing of alkali basalts. Am. Mineral. 82, 368–378.

Dixon, J.E., Stolper, E., Delaney, J.R., 1988. Infrared spectroscopic measurements of CO_2 and H_2O in Juan de Fuca Ridge basaltic glasses. Earth Planet. Sci. Lett. 90, 87–104.

Dixon, J.E., Stolper, E.M., Holloway, J.R., 1995. An experimental study of water and carbon dioxide solubilities in mid-ocean ridge basaltic liquids: Part I, Calibration and solubility models. J. Petrol. 36, 1607–1631.

Dziak, R.P., Bohnenstiehl, D.R., Matsumoto, H., Fowler, M.J., Haxel, J.H., Tolstoy, M., Waldhauser, F., 2009. January 2006 seafloor-spreading event at 9_500N, East Pacific Rise: ridge dike intrusion and transform fault interactions from regional hydroacoustic data. Geochem. Geophys. Geosyst. 10. http://dx.doi.org/10.1029/2009GC002388.

Fine, G., Stolper, E., 1986. Dissolved carbon dioxide in basaltic glasses: concentrations and speciation. Earth Planet. Sci. Lett. 76, 263–278.

Flowers, G.C., 1979. Correction of Holloway's (1977) adaption of the modified Redlich–Kwong equation of state for calculation of the fugacities of molecular species in supercritical fluids of geologic interest. Contrib. Mineral. Petrol. 69, 315–318.

Fundis, A.T., Soule, S.A., Fornari, D.J., Perfit, M.R., 2010. Paving the seafloor: volcanic emplacement processes during the 2005–06 eruption at the fast-spreading East Pacific Rise, 9°50″N. Geochem. Geophys. Geosyst. 11. http://dx.doi.org/10.1029/2010GC003058.

Gonnermann, H., Manga, M., 2005. Nonequilibrium magma degassing: results from modeling of the ca. 1340 A.D. eruption of Mono Craters, California. Earth Planet. Sci. Lett. 238, 1–16.

Gregg, T.K., Fink, J.H., 1995. Quantification of submarine lava-flow morphology through analog experiments. Geology 23, 73–76.

Gregg, T.K.P., Fornari, D.J., Perfit, M.R., Haymon, R.M., Fink, J.H., 1996. Rapid emplacement of a mid-ocean ridge lava flow on the East Pacific Rise at 9°46′–51′N. Earth Planet. Sci. Lett. 144, E1–E7.

Hanyu, T., Clague, D.A., Kaneoka, I., Dunai, T., Davies, G.R., 2005. Noble gas systematics of submarine alkali lavas near Hawaiian hotspot. Chem. Geol. 214, 135–155.

Holloway, J.R., 1977. Fugacity and activity of molecular species in supercritical fluids. In: Faser, D. (Ed.), Thermodynamics in Geology. Springer, Netherlands, pp. 161–181.

Hui, H., Zhang, Y., 2007. Toward a general viscosity equation for natural anhydrous and hydrous silicate melts. Geochim. Cosmochim. Acta 71, 403–416.

Jackson, B., Gardner, J.E., 2015. Degassing of mid-ocean ridge basalts: quantifying bubble nucleation and growth in the 2005–06 East Pacific Rise lava. Eos Trans. AGU: Fall Meet. Suppl., Abstract.

Kent, G.M., Harding, A.J., Orcutt, J.A., 1993. Distribution of magma beneath the East Pacific Rise between the Clipperton transform and the 9°17″N Deval from forward modeling of common depth point data. J. Geophys. Res. 98, 13945–13969.

Ketcham, R.A., 2005. Computational methods for quantitative analysis of three-dimensional features in geological specimens. Geosphere 1, 32–41.

Lange, R.A., 1994. The effect of H_2O, CO_2, and F on the density and viscosity of silicate melts. Rev. Mineral. Geochem. 30, 331–370.

Lensky, N., Lyakhovsky, V., Navon, O., 2001. Radial variations of melt viscosity around growing bubbles and gas overpressure in vesiculating magmas. Earth Planet. Sci. Lett. 186, 1–6.

le Roux, P.J., Shirley, S.B., Hauri, E.H., Perfit, M.R., Bender, J.F., 2006. The effects of variable sources, processes and contaminants on the composition of northern EPR MORB (8–10°N & 12–14°N): evidence from volatiles (H_2O, CO_2, S) and halogens. Earth Planet. Sci. Lett. 251, 209–231.

Ochs, F.A., Lange, R.A., 1999. The density of hydrous magmatic liquids. Science 283, 1314–1317.

Paonita, A., Martelli, M., 2006. Magma dynamics at mid-ocean ridges by noble gas kinetic fractionation: assessment of magmatic ascent rates. Earth Planet. Sci. Lett. 241, 138–158.

Perfit, M.R., Chadwick, W.W., 1998. Magmatism at mid-ocean ridges: constraints from volcanological and geochemical investigations. In: Buck, W.R., Delaney, J.R., Karson, J.A., Lagabrielle, Y. (Eds.), Faulting and Magmatism at Mid-Ocean Ridges. AGU, Washington, DC, pp. 59–116.

Proussevitch, A.A., Sahagian, D., 1998. Dynamics and energetics of bubble growth in magmas: analytical formulation and numerical modeling. J. Geophys. Res. 103, 18223–18251.

Sarda, P., Graham, D., 1990. Mid-ocean ridge popping rocks: implications for degassing at ridge crests. Earth Planet. Sci. Lett. 97, 268–289.

Shaw, A.M., Behn, M.D., Humphris, S.E., Sohn, R.A., Gregg, P.M., 2010. Deep pooling of low degree melts and volatile fluxes at the 85°E segment of the Gakkel Ridge: evidence from olivine-hosted melt inclusions and glasses. Earth Planet. Sci. Lett. 289, 311–322.

Simons, K., Dixon, J., Schilling, J.G., Kingsley, R., Poreda, R., 2002. Volatiles in basaltic glasses from the Easter-Salas y Gomez Seamount Chain and Easter Microplate:

implications for geochemical cycling of volatile elements. Geochem. Geophys. Geosyst. 3. http://dx.doi.org/10.1029/2001GC000173.

Soule, S.A., Fornari, D.J., Perfit, M.R., Rubin, K.H., 2007. New insights into mid-ocean ridge volcanic processes from the 2005–2006 eruption of the East Pacific Rise, 9°46′N–9°56′N. Geology 35, 1079–1082.

Soule, S.A., Nakata, D.S., Fornari, D.J., Fundis, A.T., Perfit, M.R., Kurz, M.D., 2012. CO_2 variability in mid-ocean ridge basalts from syn-emplacement degassing: constraints on eruption dynamics. Earth Planet. Sci. Lett. 327, 39–49.

Soule, S.A., Fornari, D.J., Perfit, M.R., Tivey, M.A., Ridley, W.I., Schouten, H., 2005. Channelized lava flows at the East Pacific Rise crest 9–10°N: the importance of off-axis lava transport in developing the architecture of young oceanic crust. Geochem. Geophys. Geosyst. 6. http://dx.doi.org/10.1029/2005GC000912.

Staudigel, H., Gee, J., Tauxe, L., Varga, R.J., 1992. Shallow intrusive directions of sheeted dikes in the Troodos ophiolite: anisotropy of magnetic susceptibility and structural data. Geology 20, 841–844.

Stewart, M.A., Klein, E.M., Karson, J.A., 2002. Geochemistry of dikes and lavas from the north wall of the Hess Deep Rift: insights into the four-dimensional character of crustal construction at fast spreading mid-ocean ridges. J. Geophys. Res. 107, 2238. http://dx.doi.org/10.1029/2001JB000545.

Tolstoy, M., et al., 2006. A sea-floor spreading event captured by seismometers. Science 314, 1920–1922.

Zhang, Y., Ni, H., 2010. Diffusion of H, C, and O components in silicate melts. Rev. Mineral. Geochem. 72, 171–225.